Chinese Journal of Chemical Engineering 53 (2023) 270–279

Contents lists available at ScienceDirect

Chinese Journal of Chemical Engineering

journal homepage: www.elsevier.com/locate/CJChE

Full Length Article

Improving the energy efficiency of surface dielectric barrier discharge devices for plasma nitric oxide conversion utilizing active flow control

An Wang [1,2], Zhongyu Hou [1,*]

[1] National Key Laboratory of Science and Technology on Micro/Nano Fabrication, Shanghai Jiao Tong University, Shanghai 200240, China
[2] Department of Micro/Nano Electronics, School of Electronic Information and Electrical Engineering, Shanghai Jiao Tong University, Shanghai 200240, China

ARTICLE INFO

Article history:
Received 1 December 2021
Received in revised form 5 March 2022
Accepted 9 March 2022
Available online 18 March 2022

Keywords:
Flue gas
Radical
Oxidation
Surface dielectric barrier discharge (SDBD)
Plasma aerodynamic effect
Plasma NO conversion

ABSTRACT

Improving energy efficiency in plasma NO removal is a critical issue. When the surface dielectric barrier discharge (SDBD) device is considered as a combination of multiple plasma actuators, the induced plasma aerodynamic effect cannot be ignored, which can affect the mass transfer, then affect the chemical reactions. Five SDBD devices with different electrode arrangements are studied for NO conversion. They correspond to different flow patterns. We find that the energy efficiency in an SDBD device with a common structure (Type 1) is 28% lower than that in SDBD devices with a special arrangement (Types 2–5). Two reasons may explain the results. First, fewer active species are produced in Type 1 because the development of discharge is hindered by the mutually exclusive electric field forces caused by the symmetrically distributed charged particles. Second, the plasma wind induced by the plasma actuator can enhance the mass and heat transfer. The mixing of reactants and products is better in Types 2–5 than Type 1 due to higher turbulence kinetic energy.

1. Introduction

The burning of fossil fuels produces a large amount of NO_x every year [1–3]. NO_x can damage the respiratory system of humans and animals [4]. Acid rain formed by NO_x corrodes buildings and endangers organisms [5,6]. As a result, many countries have set increasingly strict standards for NO_x emissions [7]. Numerous methods have been studied to control it [8–14]. Low temperature plasma has a wide range of applications, such as the preparation of Au and Pd nanoparticles [15], gas purification [16,17], reforming of dimethyl ether to produce hydrogen [18], degradation of acid orange 7 (AO7) dye [19], removal of benzene [20], and plasma-assisted ignition [21]. Surface dielectric barrier discharge (SDBD) is a method of generating low temperature plasma, which has been widely used in NO removal [22–27]. Plasma oxidation dominates in oxygen-rich environments. NO is a gas difficult to be removed directly, while NO_2 is much easier to handle. Plasma removal of NO is therefore usually divided into two steps. Plasma converts NO into NO_2 in the first step and utilizes other methods to remove NO_2 in the second step. Electricity accounts for a large part of the cost of plasma NO removal [28], so reducing its energy consumption will make this technology more economical and more marketable.

An SDBD device usually consists of a high-voltage electrode, a dielectric barrier, and a ground electrode [23,25,26,29–31]. The high-voltage electrode and the ground electrode are closely attached to both sides of the dielectric barrier. High-voltage electrodes are usually metal strips, and the ground electrode is usually a whole metal plate. Above the ground electrode, the high-voltage electrodes are equally spaced. Recently, a hybrid volume-surface DBD device is proposed to get a better performance [32]. Another type of SDBD device is cylindrical [22,27]. It is composed of an external ground electrode, an internal high-voltage electrode, and a dielectric barrier in the middle. Unlike the previous, the high-voltage electrode is a spiral metal wire. In these two types of reactors, the discharge area is distributed on both sides of the high-voltage electrode.

Plasma actuators are used as an active flow control method, which has been widely studied in aviation. The plasma actuator includes an exposed electrode and an embedded electrode as shown in Fig. 1(a). Then, the common SDBD device can be viewed as a combination of many plasma actuators as shown in Fig. 1(b). The plasma actuator can produce a plasma wind with a velocity of several meters per second, which flows from the exposed electrode to the embedded electrode. The wind can affect the mass transfer, then further affects the chemical reactions. In our

* Corresponding author.
E-mail address: zhyhou@sjtu.edu.cn (Z. Hou).

https://doi.org/10.1016/j.cjche.2022.03.002
1004-9541/

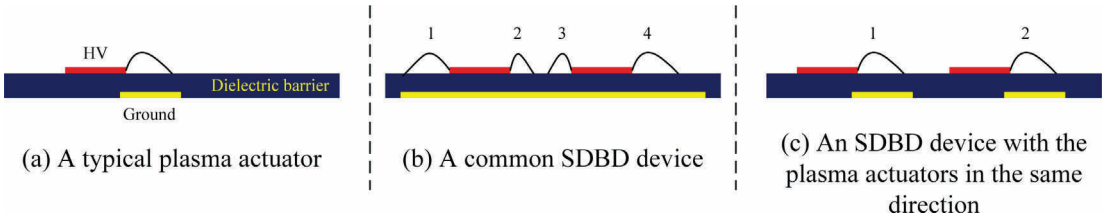

Fig. 1. Schematic diagrams of SDBD devices.

previous research, different flow patterns induced by the plasma aerodynamic effect were found to have different conversion efficiencies and energy efficiency [33]. The plasma aerodynamic effect on chemical reactions caused by the plasma actuator cannot be ignored.

In this study, we compare the performance of five types of SDBD devices for ozone production and NO conversion. In Type 1, electrodes are arranged in a common way as shown in Fig. 1(b). Two exposed electrodes and the ground electrode form four plasma actuators whose direction is not consistent. In Type 2, the electrodes are arranged as shown in Fig. 1(c). The plasma actuators 1 and 2 are in the same direction. Types 3–5 are shown in Fig. 2. The number of plasma actuators is four in Types 3–5. The distances between plasma actuators in Types 3–5 are 2, 5, and 10 mm, respectively. Plasma actuators are in the same direction in Types 3–5. The effect of air gap is also studied.

2. Methods

2.1. Reactor

2.1.1. SDBD devices

In this study, five types of SDBD devices were studied, namely Types 1–5 (Fig. 2). As shown in Fig. 2, Type 1 has a common structure among the five types. And the directions of the plasma actuators are different. In Types 2–5 there is a certain distance between the plasma actuators. And the plasma actuators are in the same direction.

All SDBD devices have a dielectric barrier in the middle and copper electrodes on either side. The material of the dielectric barrier is FR-4. The length and the width are both 100 mm, and the thickness is 1 mm.

All high voltage electrodes and ground electrodes are made of copper. They are 0.05 mm thick. In the Fig. 2, the high voltage electrode is indicated by a narrow yellow vertical bar. The length and the width of the high voltage electrodes (H1 and H2) are 80 mm and 2 mm in all the five SDBD devices.

The ground electrode (G1) of Type 1 is 76 mm long and 19 mm wide. The distance between the high-voltage electrodes is 5 mm in Type 1. The distance between the edge of the ground electrode and the high-voltage electrode is 5 mm, too. Ground electrodes of Types 2–5 (G2) are 6 mm wide and 76 mm long. The high-voltage electrode and the ground electrode overlap by 1 mm in the vertical direction. Hence, the distance between the high-voltage electrode and the edge of the ground electrode is 5 mm, too. Thus, the width of the ground electrode in each plasma actuator in Types 1–5 is the same. This ensures their similarity in discharge.

There are two plasma actuators in Type 2. The distance between the two plasma actuators is 5 mm. There are four plasma actuators in Types 3–5. Distances between plasma actuators in Types 3–5 are 2, 5, and 10 mm, respectively. The actual pictures of SDBD devices are in Fig. 3.

2.1.2. Reaction cavity

The SDBD device is placed at the bottom of a cuboid made of four acrylic plates (Fig. 4(b)). The outer width of the cuboid is 104 mm, the outer height is 16 mm, and the length is 100 mm. The acrylic plates on the left and right sides are 2 mm thick. The acrylic plates on the upper and lower sides are 5 mm thick. The height of the internal cavity is 6 mm. After placing the SDBD device, the remaining air gap is marked as *H*. *H* is in the range of 5–25 mm in this study. In Types 2–5, the direction of the plasma wind and the inlet airflow is opposite (Fig. 4(b)).

2.2. Measurement methods

2.2.1. Electrical measurement

Electrical signals are measured by an oscilloscope (Keysight EDUX1002A, USA). The AC power supply is manufactured by Trek (Model 615-10, USA). The voltage is obtained through a built-in 1000:1 voltage divider of the power supply. The current is obtained by measuring the voltage drop across a 220 Ω resistor.

2.2.2. Flow field simulation

Particle image velocimetry (PIV) is used to determine the velocity field distribution near a single plasma actuator in quiescent air. The thickness of the reactor is 5–25 mm, which is not in the range

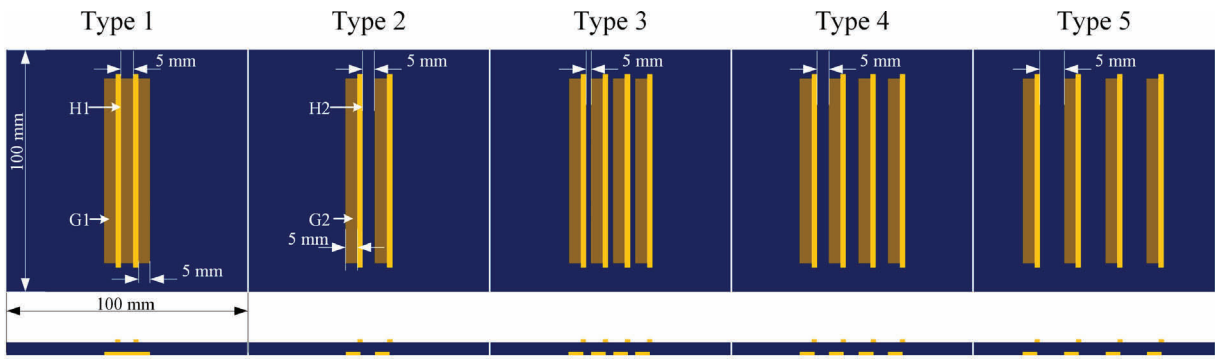

Fig. 2. Structure of SDBD devices.

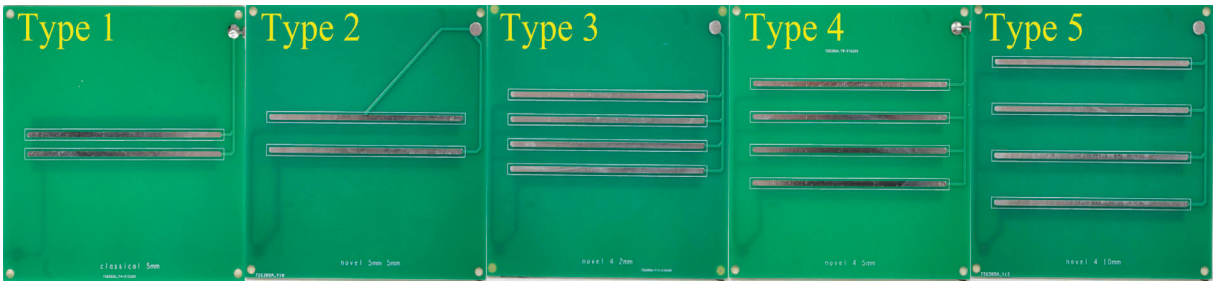

Fig. 3. Physical pictures of SDBD devices.

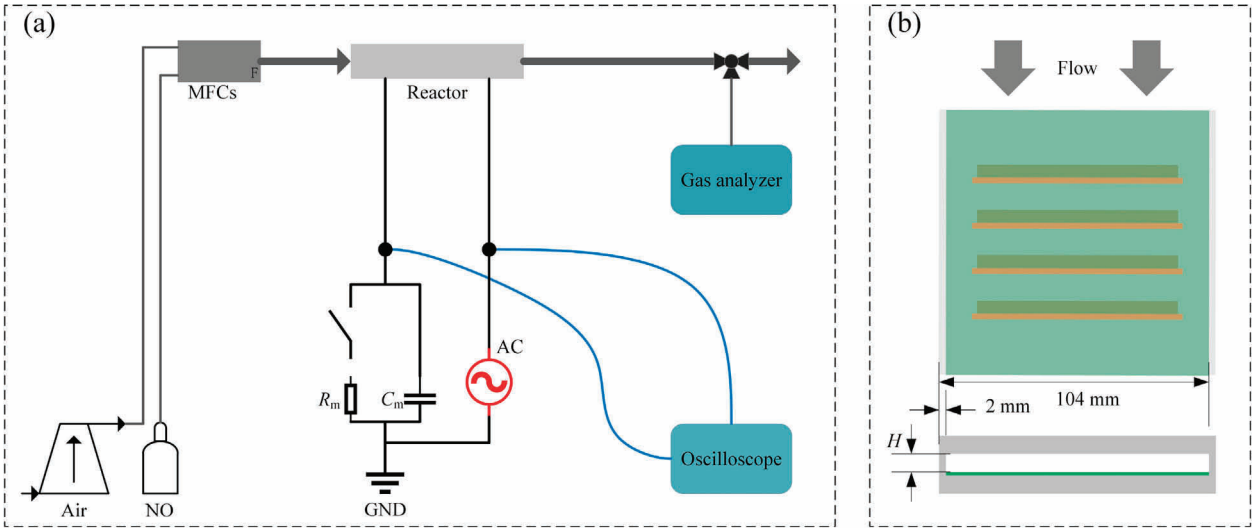

Fig. 4. Schematic of (a) the experimental setup and (b) the reactor with SDBD devices inside.

suitable for our PIV cameras. It seems too small at the distance at which the camera of our PIV system can focus. A transparent acrylic container of 200 mm × 200 mm × 200 mm is used to contain the electrode. Bubbles act as tracer particles. After the tracer particles in the container have stabilized, a high voltage is applied. The peak-to-peak voltage and frequency are 8 kV and 10 kHz, respectively. The discharge occurs, and the plasma wind is induced. Then, PIV was used to get the velocity distribution near the electrode.

The computational fluid dynamics (CFD) model is calibrated according to the PIV experimental results. More details of the CFD model can be found in Ref. [34]. The mesh used for simulation is made by the software Ansys ICEM CFD. The discharge zone is set to 1 mm thick according to the experimental results in Ref. [35], whose experimental parameters are similar to ours. The width of the discharge area is set based on the actual discharge image. The two outer discharge areas of Type 1 are set to 3.5 mm wide. Two discharge areas in the middle of Type 1 are set to 2 mm wide. The discharge area of Types 2–5 is 3.5 mm wide. The calibrated CFD model is then used for the simulation of the flow field in this study.

2.2.3. Gas composition measurement

Simulated flue gas in this study is a mixture of NO (N_2 as a balance gas) and air (about 78% N_2, and 21% O_2). The concentration of NO to be treated is 0.4 mg·L^{-1}, and the flow rate is 3 L·min^{-1}. The NO concentration is measured by the Testo 340 (Germany). The measured NO concentration is not affected by ozone, which has been verified by Filimonova [36]. During experiments, no VOCs were detected. The O_3 concentration is measured by an ozone detector (B1010, WOST, China).

2.2.4. Capture of discharge images

The discharge images were taken with a Sony A7M2 (Japan). The shooting was conducted with an aperture of 5.6, a focal length of 70 mm, and an exposure time of 30 s at an ISO (International Organization for Standardization) of 100.

2.3. Definitions

2.3.1. Conversion efficiency

The NO conversion efficiency ϵ (%) is calculated as,

$$\epsilon = \frac{NO_i - NO_f}{NO_i} \times 100\% \quad (1)$$

where NO_i is the initial NO concentration (mg·L^{-1}), NO_f is the final NO concentration (mg·L^{-1}).

2.3.2. Energy efficiency of NO conversion

The energy efficiency of NO conversion η_{NO} (g·kWh^{-1}) is calculated as,

$$\eta_{NO} = \frac{Q \times 60 \times \Delta NO}{P} \quad (2)$$

where Q is the flow rate (L·min^{-1}), ΔNO is the NO converted (mg·L^{-1}), P is the power consumed (W).

2.3.3. Energy efficiency of O_3 production

The energy efficiency of O_3 production η_{O_3} ($g \cdot kWh^{-1}$) is calculated as,

$$\eta_{O_3} = \frac{Q \times 60 \times C_{O_3}}{P} \tag{3}$$

where Q is the flow rate ($L \cdot min^{-1}$), C_{O_3} is the produced O_3 ($mg \cdot L^{-1}$), P is the power consumed (W).

2.3.4. Turbulence kinetic energy (TKE)

TKE is defined as

$$k = \frac{u'^2 + v'^2 + w'^2}{2}, \quad u' = u - \bar{u}, \quad v' = v - \bar{v}, \quad w' = w - \bar{w} \tag{4}$$

where k is the TKE, the instantaneous velocities in the x, y, and z directions are represented by u, v, w, respectively. $\bar{u}$, $\bar{v}$, $\bar{w}$ are the average velocity.

2.3.5. Power

The consumed power can be calculated by the integral of the product of $u(t)$ and $i(t)$,

$$P(W) = \frac{1}{N}\sum_{t=1}^{N} u(t)i(t) \tag{5}$$

where $u(t)$ is the instantaneous voltage on the reactor and $i(t)$ is the filtered instantaneous current.

2.3.6. Gray value

The gray value is defined as

$$\text{Gray value} = 0.299R + 0.587G + 0.144B \tag{6}$$

where R, G, B, represent the red, green, and blue components, respectively.

2.4. Statistical methods

All electronic signals are sampled for more than 10 cycles. The concentration was measured 5 times. Error bars consist of mean and standard deviation.

3. Results

3.1. Brightness, uniformity and width of discharge

They are discharge images of Types 1–5 in Fig. 5 from left to right, respectively. From top to bottom, the discharge voltage is 6.0, 6.5, 7.0, 7.5, 8.0 kV, respectively. With 6.0 kV, the discharge is in its initial stage, and there is only a weak discharge. At 6.5 kV, the discharge becomes bright but mottled. It does not cover the whole electrode. At 7.0 kV, the entire electrode is emitting light, but a few positions are still missing. At 7.5 kV, the discharge basically reached a uniform state. At 8.0 kV, the discharge is completely uniform.

As the voltage increases, the brightness of the discharge increases. The brightness changes little after 7.0 kV. The brightness of the five SDBD devices is different at the same voltage. Types 2–5 has a gray value of 170, while Type 1 only has a gray value of 150. As the voltage rises, the discharge area tends to widen. The width of the discharge area of Types 2–5 is about 3.5 mm at 8.0 kV. The outer two discharge areas of Type 1 (plasma actuator 1 and 4 in Fig. 1(b)) are about 3.5 mm wide, and the middle two (plasma actuator 2 and 3 in Fig. 1(b)) are only about 2 mm wide.

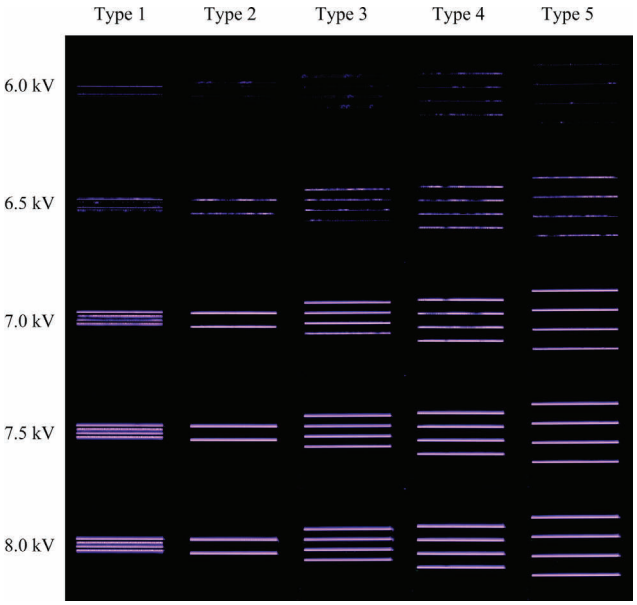

Fig. 5. Discharge images of the five SDBD devices as the voltage changes.

3.2. Typical voltage and current

Fig. 6 shows the typical discharge waveform of Types 1–5. A discharge waveform of about two cycles was recorded. Each cycle is about 0.0001 s, and the corresponding frequency is 10 kHz. The voltage and the fundamental frequency of the current have the form of a sine curve. The current waveform is accompanied by a large number of spikes. The amplitude of the spikes of the five types of discharge device reached 0.6, 0.2, 0.4, 0.4, 0.4 A, respectively. And the spikes of Type 2 are sparser than the other four. At the same time, the phase of the current waveform is ahead of the voltage waveform by about $\pi/2$, which is a typical capacitive load.

3.3. Velocity distribution

The plasma wind induced by the plasma actuator is about 1 $m \cdot s^{-1}$ in Fig. 7. The inlet airflow is about 0.1 $m \cdot s^{-1}$. The induced plasma wind has a much higher velocity than the inlet airflow. Plasma wind blows from the exposed electrode to the embedded electrode. When the plasma wind and the inlet airflow is opposite, the plasma wind first blows toward the inlet for a certain distance before being pushed toward the outlet by the inlet air pressure. This is the case for Types 2–5 and the left part of Type 1 (plasma actuator 1 and 3 in Fig. 1(b)) in Fig. 7. When the direction of the plasma wind and the inlet airflow are the same, the induced plasma wind absorbs part of the inlet airflow, then flow toward the outlet. This is the case for the right part of Type 1 (plasma actuator 2 and 4 in Fig. 1(b)) in Fig. 7.

For a single plasma actuator, the plasma wind reaches its maximum speed around the discharge area. When the induced plasma wind is opposite to the inlet airflow, the velocity is relatively large (about 0.5 $m \cdot s^{-1}$) in the range of about 10 mm wide and about 5 mm high with the electrode as the center in Types 2–5 and the left part of Type 1 in Fig. 7. This entire area is irregularly elliptical. When the induced plasma wind is in the same direction as the inlet airflow, the discharge area is about 2 mm toward the inlet, about 6 mm toward the outlet direction, and about 2 mm high, and the velocity value is about 0.5 $m \cdot s^{-1}$ in the right part of Type 1 in Fig. 7. The entire area is obliquely long. When the plasma wind

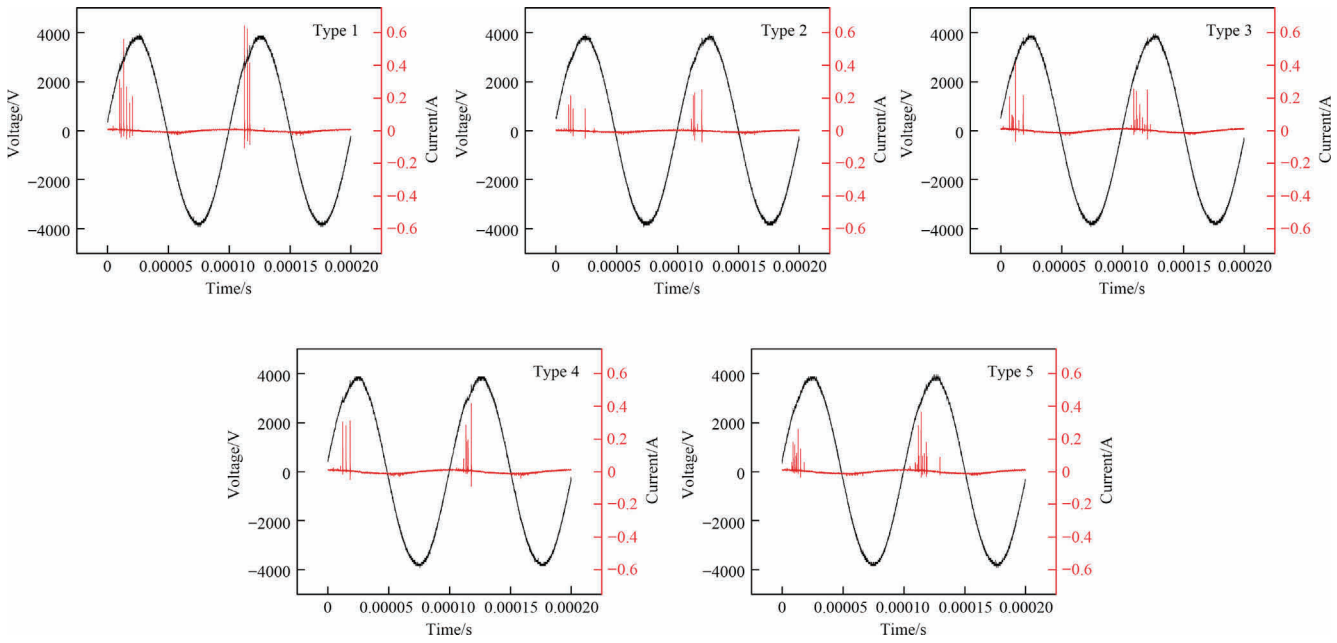

Fig. 6. Typical discharge voltage and current of Types 1–5 at 8.0 kV, 10 kHz. (The NO concentration is 0.4 mg·L^{-1}. The flow rate is 3 L·min^{-1}. Discharge occurs at room temperature.)

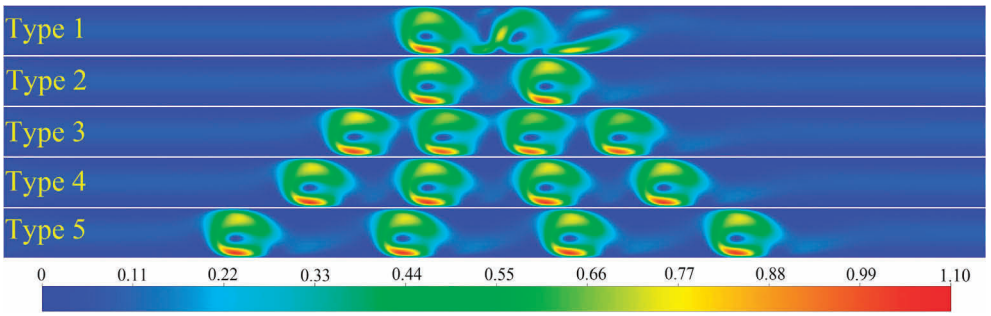

Fig. 7. Velocity distributions (m·s^{-1}) of five types of discharge devices at 8.0 kV, 3 L·min^{-1}. The air gap is 5 mm.

and inlet gas flow are opposite, there is a larger discharge area than when they are the same.

As a whole, the direction of plasma wind and inlet gas flow in Types 2–5 is opposite, and the velocity distribution around each discharge area is similar. The only difference is the distance between plasma actuators. Type 3 has a short distance, and the plasma wind induced by four plasma actuators seems to be connected. In Type 1, the common SDBD device, plasma wind induced by two discharge areas are identical to inlet gas flow in direction, and the other two are opposite. As a result, its velocity distribution is very different from Types 2–5.

3.4. TKE distribution

The TKE of all five SDBD devices reaches 0.35 m^2·s^{-2} in the discharge area (Fig. 8). The TKE is higher than 0.15 m^2·s^{-2} in a large area. As the distance from the discharge area increases, the TKE decreases. Areas with high TKE are formed around the plasma actuator.

When the plasma wind and the inlet flow are opposite, irregular elliptical areas with high TKE is formed around the electrode, such as the leftmost discharge area in Type 1 and all discharge areas in Types 2–5. The area reaches the upper wall of the reactor. The height is about 5 mm, and the width is about 10 mm. When the plasma wind and the inlet flow are in the same direction, the high TKE area formed around the electrode is inclined and flat, such as the rightmost in Type 1. The width of this area is 10 mm, but the height is only 2 mm. The area with high TKE is much larger when the plasma wind and the inlet flow are in opposite directions than in the same direction.

The area with high TKE is small in the middle two discharge areas of Type 1 (plasma actuator 2 and 3 in Fig. 1(b)) because the two plasma actuators are opposite. The plasma wind induced by two plasma actuators is opposite and cancels each other out. TKE is small in the right area of Type 1 due to these factors. In Types 2–5, the distribution of TKE is similar. Only in Type 3, the discharge areas seem to be connected together due to their short distance.

3.5. The average TKE of the five SDBD devices

Since the number of plasma actuators for each type of SDBD devices is not consistent, the total TKE is divided by the number of plasma actuators to get an average value. The results are shown in Fig. 9. It shows that the average TKE in Type 1 is only about 250 m^2·s^{-2}, while the TKE in Types 3–5 reaches about 450 m^2·s^{-2}. Type 2 is the highest and reaches 550 m^2·s^{-2}. This can also be seen from the Fig. 8 that the high TKE area of Type 1 is smaller than that of Types 2–5.

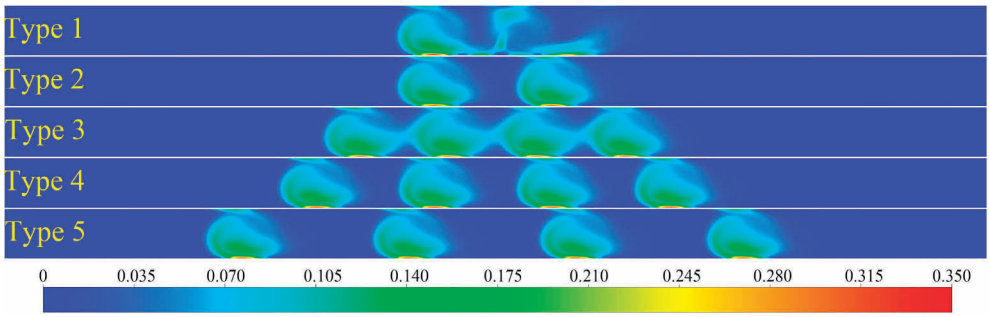

Fig. 8. TKE distributions ($m^2 \cdot s^{-2}$) of five types of discharge devices at 8.0 kV, 3 $L \cdot min^{-1}$. The air gap is 5 mm.

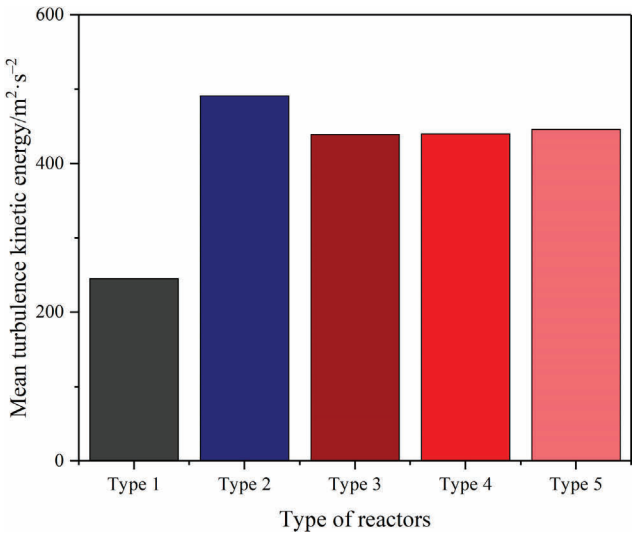

Fig. 9. Mean TKE of five types of discharge devices.

3.6. The effect of air gap on ozone production

Fig. 10 shows the effect of air gap and reactor type on ozone production. The air gap means the distance between the upper wall of the reactor and the plasma actuator, which is marked as *H* in Fig. 4. The concentration of the produced ozone of Types 1, 3, 4, and 5 is about 1.2 $mg \cdot L^{-1}$ with a 5 mm air gap. That of Type 2 is about 0.7 $mg \cdot L^{-1}$. The possible reason is that it only has two plasma actuators while others have four. The ozone production of Types 1–5 decreases approximately linearly with an increasing air gap, which is similar to results in Ref. [32]. The possible reason is that with the increase of the air gap, the proportion of gas in contact with the discharge area becomes smaller. Then it leads to a smaller probability of collision between the O_2 and the active species. Finally, it leads to a decrease in ozone production.

Fig. 11 shows the effect of air gap and reactor type on the energy efficiency of ozone production. When the air gap is 5 mm, the energy efficiency of Types 2–5 for ozone production is about 100 $g \cdot kWh^{-1}$. The energy efficiency is less than 80 $g \cdot kWh^{-1}$ for Type 1 with the same air gap. It decreases approximately linearly with an increasing air gap due to the same reason described in the previous paragraph.

3.7. The effect of air gap on NO conversion

Fig. 12 shows the effect of air gap and reactor type on NO conversion. The conversion efficiency of Types 1, 3, 4, and 5 reached about 80% when the air gap is 5 mm. The distance between the plasma actuators seems not to have a significant effect on the conversion efficiency and discharge power of Types 3–5. Among them,

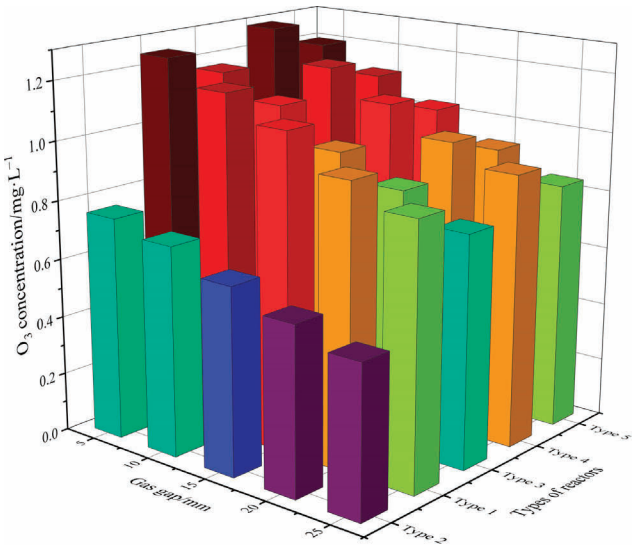

Fig. 10. The ozone production as a function of reactor type and air gap. The voltage is 8.0 kV. The frequency is 10 kHz. The flow rate is 6 $L \cdot min^{-1}$. Discharge occurs at room temperature. Note that the order of the five reactors is Type 2, Type 1, Type 3, Type 4, Type 5 so that Type 2 is not blocked.

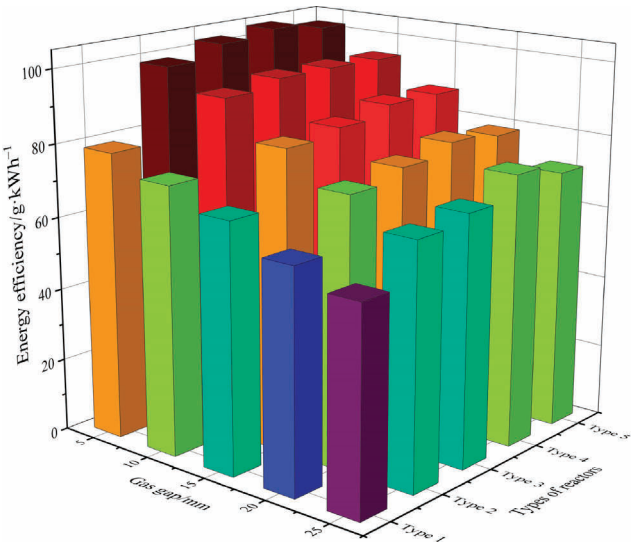

Fig. 11. The energy efficiency of ozone production as a function of reactor type and air gap. The voltage is 8.0 kV. The frequency is 10 kHz. The flow rate is 6 $L \cdot min^{-1}$. Discharge occurs at room temperature.

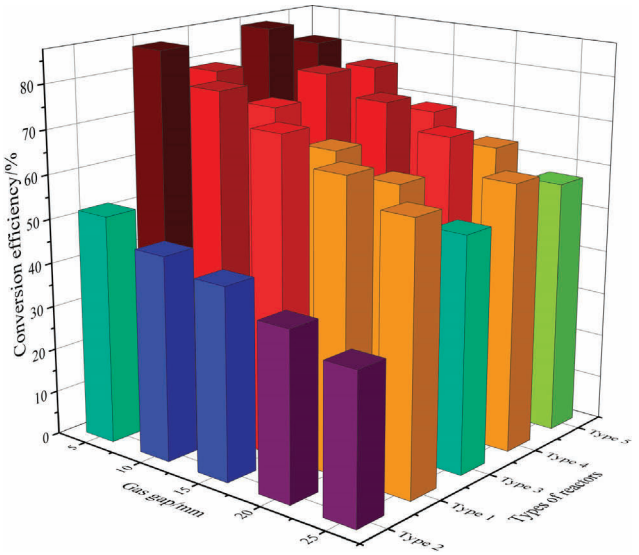

Fig. 12. The conversion efficiency of NO as a function of reactor type and air gap. The voltage is 8.0 kV. The frequency is 10 kHz. The concentration is 0.4 mg·L^{-1}. The flow rate is 3 L·min^{-1}. Discharge occurs at room temperature. Note that the order of the five reactors is Type 2, Type 1, Type 3, Type 4, Type 5 so that Type 2 is not blocked.

the conversion efficiency of Types 1 and 4 reaches higher than 85%. However, the power consumption of these two is also the highest, reaching about 3 and 2.3 W, respectively. Types 3 and 5 have slightly lower power than Type 4. The conversion efficiency of Type 2 is about 50% with the same air gap. Type 2 has only two plasma actuators, and it has the lowest discharge power. The conversion efficiency of Types 1–5 decreases approximately linearly with an increasing air gap. For example, the conversion efficiency of Type 1 is about 85% with a air gap of 5 mm. It reduces to about 60% when the air gap is 25 mm.

Fig. 13 shows the effect of air gap and reactor type on the energy efficiency of NO conversion. When the air gap is 5 mm, the energy efficiency of Types 2–5 is about 23 g·kWh^{-1}. The distance between plasma actuators and the number of plasma actuators has little effect on the energy efficiency of Types 2–5. The energy efficiency is only about 18 g·kWh^{-1} for Type 1 with the same air gap. The energy efficiency of Types 2–5 is 28% higher than that of Type 1. It decreases approximately linearly with an increasing air gap as a result of a decrease in conversion efficiency.

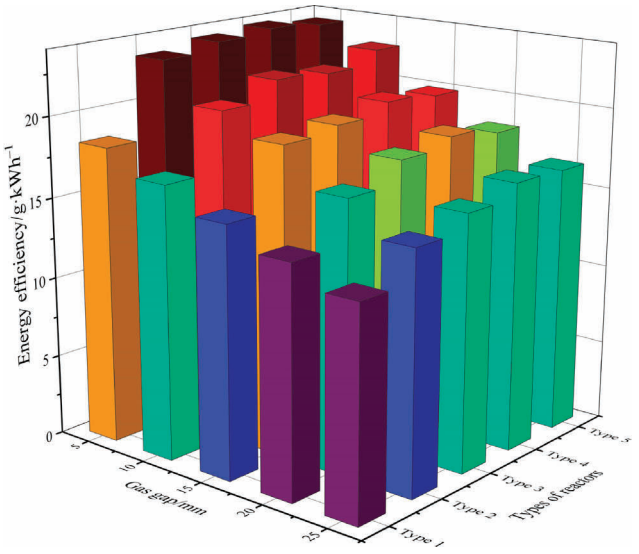

Fig. 13. The energy efficiency of NO conversion as a function of reactor type and air gap. The voltage is 8.0 kV. The frequency is 10 kHz. The concentration is 0.4 mg·L^{-1}. The flow rate is 3 L·min^{-1}. Discharge occurs at room temperature.

4. Discussion

The plasma NO conversion can be affected by the flow field and the electric field. The flow field can affect the distribution of reactants and products, thereby affecting the chemical reactions. It can also affect the distribution of some heavy-charged particles, thereby affecting the discharge. The gas discharge is affected by the drag force of airflow and the electrostatic force at atmospheric pressure, which has been validated in Ref. [37].

The flow field is affected by the inlet airflow and the wind induced by the plasma actuator. Compared to a single plasma actuator, SDBD devices with multiple plasma actuators present two new characteristics. One is that the charged particles inside the adjacent discharge areas in common SDBD devices affect each other, thereby affecting the internal electric field, and then affecting the discharge. The second is that the flow field in the reactor is affected not only by the inlet airflow and the plasma wind induced by one plasma actuator but also by the interaction between the plasma winds induced by multiple plasma actuators.

4.1. The development of discharge is hindered by mutually exclusive charged particles in the two adjacent discharge areas in common SDBD devices like Type 1

In Fig. 5, the width of the two discharge areas in the middle of Type 1 is about 2 mm. The width of the two discharge areas on the two outer sides in Type 1 is about 3.5 mm. The former is smaller than the latter. In Type 1, the discharge area on the two outer sides is similar in width to the discharge area in Types 2–5. The two plasma actuators in the middle of Type 1 (plasma actuator 2 and 3 in Fig. 1(b)) are in opposite directions. The plasma actuators in Types 2–5 are in the same direction.

Positive ions and free electrons are generated in the discharge area after a discharge. When positive high voltage is applied on the exposed electrode, because electrons move at two orders of magnitude faster than positive ions, they reach the exposed anode first, while positive ions remain in the discharge area. When negative high voltage is applied on the exposed electrode, electrons accumulate on the surface of the dielectric barrier above the ground electrode, and positive ions are distributed in the discharge area after a discharge (Fig. 14) [37].

Thus, the distribution of charged particles in the two adjacent discharge areas in the middle of Type 1 is similar. The same kind of charges generates a mutually exclusive force, hindering the development of the discharge. In Ref. [37], a significant mutual repulsion phenomenon is observed between two discharge filaments at a distance of 10 mm. In that paper, the electric field force near the discharge area is greater than the drag force of the airflow and plays a dominant role. As the number of HV electrodes increases in common SDBD devices like Type 1, most discharge areas will be in the state the same as plasma actuator 2 and 3 in Type 1. In other words, they are in a state where the development of the discharge is hindered. The same phenomenon could also be found in Ref. [29], where two adjacent discharge areas cannot fuse together even at a high voltage.

In Types 2–5, the distributions of charged particles in different discharge areas are arranged in the same direction as shown in Fig. 14, which is beneficial to the development of discharge. In Type 1, the development of discharge is hindered by the mutually exclusive charged particles formed by discharge. As a result, fewer active species are formed in SDBD devices like Type 1, which neg-

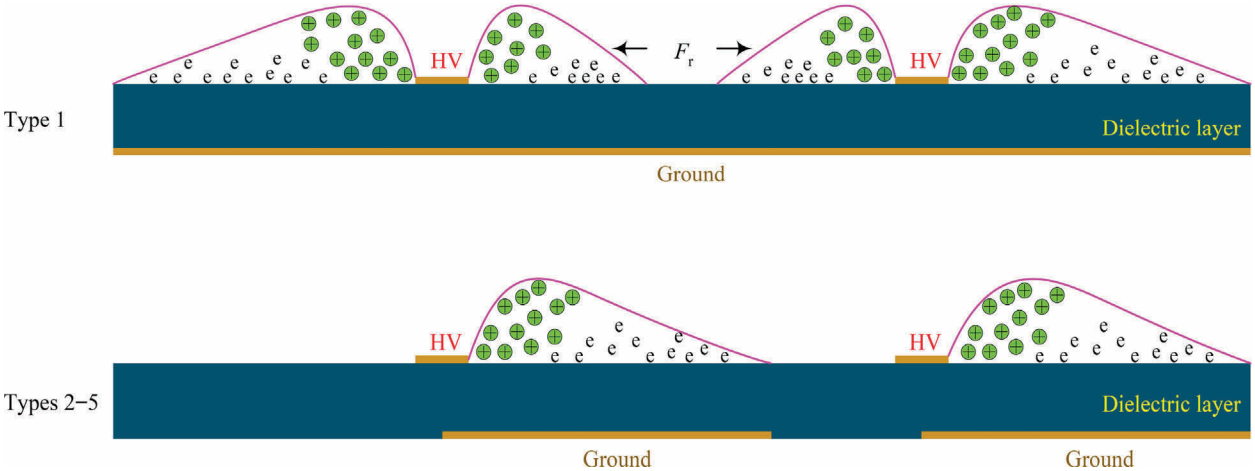

Fig. 14. Schematic diagram of the distribution of charged particles in SDBD devices. The electron is represented by the letter 'e'. The positive charge is indicated by green circles with a positive sign inside. The mutually exclusive electric field force between two adjacent discharge areas is represented by F_r.

atively affects the chemical reactions. In summary, SDBD devices like Types 2–5 are more beneficial to the development of discharge and can facilitate chemical reactions.

4.2. The improvement of energy efficiency of NO conversion caused by the plasma aerodynamic effect

Before discharge, the initial gas composition is uniformly distributed throughout the reactor. When discharge occurs, various active species are produced in the discharge area. These active species will decay in several microseconds. Thus, most of the active species are limited in the discharge area. At the same time, the reaction products like O_3 and NO_2 can live much longer, follow the airflow, and move out of the discharge area. The distribution of reactants and the products are not uniform.

The plasma wind induced by the plasma actuator can enhance the mass and heat transfer [38]. The plasma wind is found to reduce the effective thickness of the gas/liquid boundary layer, enhance the mixing between active species and pollutants, and increase the absorption of SO_2 [39–41]. The enhancement is stronger at a higher TKE. In this study, the aerodynamic effect induced by the plasma actuator enhances the mass transfer, then weakens the uneven distribution of reactants and production, thereby promoting NO conversion and ozone production. Types 2–5 has a higher TKE than Type 1, which means a better mixing ability. That is possibly why the performance of Types 2–5 is better than that of Type 1.

4.3. The influence of the distance between the plasma actuators and number of plasma actuators in SDBD devices like Types 2–5

Fig. 13 shows that for Types 3–5, the distance between plasma actuators increased from 2 mm to 10 mm, but the energy efficiency did not change much. For Type 2 and Type 4, the increase in the number of plasma actuators has little effect on energy efficiency. However, in Fig. 9, Type 2 has higher average TKE than Type 4. The statistics here are the sum of TKE in the entire reactor. Aside from the discharge area having the strongest TKE, it also contains other areas with weaker TKE. If the value of this part is T_{others}, the TKE generated by each plasma actuator is T_{elec}. For an SDBD devices with two plasma actuators, the average TKE is $T_{others}/2$ +- T_{elec}. For an SDBD devices with four plasma actuators, the average TKE is $T_{others}/4 + T_{elec}$. The average TKE of the former is naturally higher than that of the latter. As a result, the TKE for each plasma actuator is similar.

Therefore, the distance between the plasma actuators and the number of the plasma actuators have little effect on their energy efficiency, which provides the potential for the expansion of this kind of SDBD device.

5. Conclusions

Surface dielectric barrier discharge (SDBD) is a promising way to remove harmful substances and produce ozone. Electrodes in the SDBD device can be seen as plasma actuators. Then the SDBD device can be considered to consist of many plasma actuators. Plasma actuators can induce plasma wind and affect mass and heat transfer, then affect the chemical reactions. The interactions between charged particles in discharge areas produced by different plasma actuators can affect the internal electric field.

In this study, five SDBD devices with different electrode arrangements are studied for NO conversion and ozone production. We find that the energy efficiency in an SDBD device with a common structure (Type 1) is about 28% lower than that in SDBD devices with special arrangement (Types 2–5). Two reasons may explain the results. First, the width of the discharge area in Type 1 is about 2 mm, while it is about 3.5 mm in Types 2–5, which results in fewer active species being produced. Because the charged particles are symmetrically distributed in the common SDBD device, they produce mutually exclusive electric field forces which hinder the development of discharge. Second, the mass transfer in Types 2–5 is stronger than that in Type 1 because the TKE in Types 2–5 is higher than that of Type 1, which means a better mixing ability of the reactants and products.

Data Availability

Data will be made available on request.

Declaration of Competing Interest

The authors declare that they have no known competing financial interests or personal relationships that could have appeared to influence the work reported in this paper.

Acknowledgements

This work was financially supported by the National Natural Science Foundation of China (60906053, 61204069, 61274118,

61306144, 61504079, and 11605112), Scientific and Innovative Action Plan of Shanghai (15DZ1160800 and 17XD1702400), China Postdoctoral Science Foundation (2016 M601595).

References

[1] F. Liu, S. Beirle, Q. Zhang, R.J. van der A, B. Zheng, D. Tong, K.B. He, NO_x emission trends over Chinese cities estimated from OMI observations during 2005 to 2015, *Atmos. Chem. Phys.* 17 (15) (2017) 9261–9275.

[2] J.L. Jimenez, G.J. McRae, D.D. Nelson, M.S. Zahniser, C.E. Kolb, Remote sensing of NO and NO_2 emissions from heavy-duty diesel trucks using tunable diode lasers, *Environ. Sci. Technol.* 34 (12) (2000) 2380–2387.

[3] J.L. Laughner, R.C. Cohen, Direct observation of changing NO_x lifetime in North American cities, *Science* 366 (6466) (2019) 723–727.

[4] A.D. Bergstra, B. Brunekreef, A. Burdorf, The effect of industry-related air pollution on lung function and respiratory symptoms in school children, *Environ. Health* 17 (1) (2018) 30.

[5] S. Ozaki, The effect of increase of NO_x and CO_2 on grain and fish production, protection of global warming and climate, *Int. J. Earth Sci. Geol.* 1 (1) (2018) 41–45.

[6] F. Corvo, J. Reyes, T. Pérez, A. Castañeda, Role of NO_x in materials corrosion and degradation, *Revista CENIC. CienciasQuìmicas* 41 (2010) 1–10.

[7] T. Ma, K. Takeuchi, Technology choice for reducing NO_x emissions: An empirical study of Chinese power plants, *Energy Policy* 102 (2017) 362–376.

[8] V.I. Pârvulescu, P. Grange, B. Delmon, Catalytic removal of NO, *Catal. Today* 46 (4) (1998) 233–316.

[9] T. Maggos, J.G. Bartzis, P. Leva, D. Kotzias, Application of photocatalytic technology for NO_x removal, *Appl. Phys. A* 89 (1) (2007) 81–84.

[10] A. Mizuno, R. Shimizu, A. Chakrabarti, L. Dascalescu, S. Furuta, No_x removal process using pulsed discharge plasma, *IEEE Trans. Ind. Appl.* 31 (5) (1995) 957–962.

[11] I. Nakamura, N. Negishi, S. Kutsuna, T. Ihara, S. Sugihara, K. Takeuchi, Role of oxygen vacancy in the plasma-treated TiO_2 photocatalyst with visible light activity for NO removal, *J. Mol. Catal. A Chem.* 161 (1–2) (2000) 205–212.

[12] L. Gao, C.T. Li, S.H. Li, W. Zhang, X.Y. Du, L. Huang, Y.C. Zhu, Y.B. Zhai, G.M. Zeng, Superior performance and resistance to SO_2 and H_2O over CoO_x-modified MnO_x/biomass activated carbons for simultaneous Hg^0 and NO removal, *Chem. Eng. J.* 371 (2019) 781–795.

[13] T. Wang, H.Z. Liu, X.Y. Zhang, Y.H. Guo, Y.S. Zhang, Y. Wang, B.M. Sun, A plasma-assisted catalytic system for NO removal over CuCe/ZSM-5 catalysts at ambient temperature, *Fuel Process. Technol.* 158 (2017) 199–205.

[14] H.Y. Xi, S. Zhou, J.X. Zhou, New experimental results of NO removal from simulated marine engine exhaust gases by $Na_2S_2O_8$/urea solutions, *Chem. Eng. J.* 362 (2019) 12–20.

[15] Z. Wang, Y. Zhu, A simple plasma reduction for synthesis of Au and Pd nanoparticles at room temperature, *Chin. J. Chem. Eng.* 23 (6) (2015) 1060–1063.

[16] L.W. Huang, Y.X. Dang, Removal of SO_2 and NO_x by pulsed corona combined with *in situ* $Ca(OH)_2$ absorption, *Chin. J. Chem. Eng.* 19 (3) (2011) 518–522.

[17] L. Yang, X. Zhang, Q. Kan, B.R. Zhao, X.X. Ma, Effect of gas composition on nitric oxide removal from simulated flue gas with DBD-NPC method, *Chin. J. Chem. Eng.* 27 (12) (2019) 3017–3026.

[18] B.W. Wang, Q.M. Sun, Y.J. Lü, M.L. Yang, W.J. Yan, Steam reforming of dimethyl ether by gliding arc gas discharge plasma for hydrogen production, *Chin. J. Chem. Eng.* 22 (1) (2014) 104–112.

[19] K.F. Shang, X.J. Wang, J. Li, H. Wang, N. Lu, N. Jiang, Y. Wu, Synergetic degradation of Acid Orange 7 (AO7) dye by DBD plasma and persulfate, *Chem. Eng. J.* 311 (2017) 378–384.

[20] K.F. Shang, J.Y. Ren, Q. Zhang, N. Lu, N. Jiang, J. Li, Successive treatment of benzene and derived byproducts by a novel plasma catalysis-adsorption process, *J. Environ. Chem. Eng.* 9 (4) (2021) 105767.

[21] X.Q. Mao, G.X. Li, Q. Chen, Y.J. Zhao, Kinetic effects of nanosecond discharge on ignition delay time, *Chin. J. Chem. Eng.* 24 (12) (2016) 1719–1727.

[22] J.T. An, Y.Z. Jiang, Z.J. Zhang, X.X. Ma, T.C. Wang, K.F. Shang, J. Li, Oxidation characteristics of mixed NO and Hg^0 in coal-fired flue gas using active species injection generated by surface discharge plasma, *Chem. Eng. J.* 288 (2016) 298–304.

[23] A.A. Abdelaziz, T. Seto, M. Abdel-Salam, Y. Otani, Performance of a surface dielectric barrier discharge based reactor for destruction of naphthalene in an air stream, *J. Phys. D Appl. Phys.* 45 (11) (2012) 115201.

[24] A.A. Abdelaziz, T. Ishijima, N. Osawa, T. Seto, Quantitative analysis of ozone and nitrogen oxides produced by a low power miniaturized surface dielectric barrier discharge: Effect of oxygen content and humidity level, *Plasma Chem. Plasma Process.* 39 (1) (2019) 165–185.

[25] S. Chen, T. Wang, H.Q. Wang, Z.B. Wu, Insights into the reaction pathways and mechanism of NO removal by SDBD plasma *via* FT-IR measurements, *Fuel Process. Technol.* 186 (2019) 125–136.

[26] A.J.M. Pemen, V.R. Chirumamilla, F.J.C.M. Beckers, W.F.L.M. Hoeben, T. Huiskamp, An SDBD plasma-catalytic system for on-demand air purification, *IEEE Trans. Plasma Sci.* 46 (12) (2018) 4078–4090.

[27] B. Wang, F. Yang, Z.J. Song, L.S. Sun, Removal of Hg^0, NO, and SO_2 by the surface dielectric barrier discharge coupled with Mn/Ce/Ti-based catalyst, *Environ. Sci. Pollut. Res.* 28 (14) (2021) 17648–17658.

[28] T. Yamamoto, C.L. Yang, M.R. Beltran, Z. Kravets, Plasma-assisted chemical process for NO_x control, *IEEE Trans. Ind. Appl.* 36 (3) (2000) 923–927.

[29] M.A. Malik, K.H. Schoenbach, R. Heller, Coupled surface dielectric barrier discharge reactor-ozone synthesis and nitric oxide conversion from air, *Chem. Eng. J.* 256 (2014) 222–229.

[30] K. Nassour, M. Brahami, S. Nemmich, N. Hammadi, N. Zouzou, A. Tilmatine, New hybrid surface–volume dielectric barrier discharge reactor for ozone generation, *IEEE Trans. Ind. Appl.* 53 (3) (2017) 2477–2484.

[31] J. Jolibois, K. Takashima, A. Mizuno, Application of a non-thermal surface plasma discharge in wet condition for gas exhaust treatment: NO_x removal, *J. Electrost.* 70 (3) (2012) 300–308.

[32] K.F. Shang, M.W. Wang, B.F. Peng, J. Li, N. Lu, N. Jiang, Y. Wu, Characterization of a novel volume-surface{DBD}reactor: Discharge characteristics, ozone production and benzene degradation, *J. Phys. D Appl. Phys.* 53 (6) (2019) 065201.

[33] A. Wang, Z.Y. Hou, Reducing energy consumption in plasma NO conversion utilizing plasma aerodynamic effect, *Chem. Eng. J.* 408 (2021) 127286.

[34] T. West, S. Hosder, Numerical investigation of plasma actuator configurations for flow separation control at multiple angles of attack, in: Proceedings of the 6th AIAA Flow Control Conference, New Orleans, Louisiana, USA, 2012, p. 3053.

[35] M. Kotsonis, S. Ghaemi, L. Veldhuis, F. Scarano, Measurement of the body force field of plasma actuators, *J. Phys. D Appl. Phys.* 44 (4) (2011) 045204.

[36] E. Filimonova, F. Beckers, R. Smulders, A. Pemen, W. Hoeben, E. Van Heesch, Pulsed corona oxidation of low NO and NO_2 concentrations: Semi-industrial tests and model simulations to illustrate the process, Proceedings of the 63rd Gaseous Electronics Conference (GEC) and 7th ICRP, 2010.

[37] Z.H. Fan, H.J. Yan, Y.D. Liu, H.F. Guo, Y.Y. Wang, C.S. Ren, Investigation of airflow effects on the dielectric barrier discharge with single/double discharge channel arrangement, *Phys. Plasmas* 25 (5) (2018) 053519.

[38] R. Karami, B. Kamkari, K. Kashefi, Investigation of corona wind effect on heat and mass transfer enhancement, *Int. J. Phys. Math. Sci.* 5 (2011) 1598–1604.

[39] M. Senichi, N. Hideyuki, Control of NO_x by positive and negative pulsed corona discharges, *IEEE Trans. Ind. Appl.* 26 (1990) 374–383.

[40] K. Onda, Y. Kasuga, K. Kato, M. Fujiwara, M. Tanimoto, Electric discharge removal of SO_2 and NO_x from combustion flue gas by pulsed corona discharge, *Energy Convers. Manag.* 38 (10–13) (1997) 1377–1387.

[41] S. Khang, K. Larkin, T. Keener, S. Khang, The effect of nonthermal plasmas on mass transfer coefficients for gas cleaning, Workshop on Applications of Electrostatics for Control of Gas Phase Air Pollutants, 1997.

Appendix A. Chemical reaction processes in plasma NO conversion

The main chemical reactions that occur during plasma NO conversion are listed in this section.

$$e + O_2 \rightarrow e + O(^3p) + O(^3p) \quad (A.1)$$

$$e + O_2 \rightarrow e + O(^3P) + O(^1D) \quad (A.2)$$

$$e + N_2 \rightarrow e + N(^4S) + N(^4S) \quad (A.3)$$

$$e + N_2 \rightarrow e + N(^4S) + N(^2D) \quad (A.4)$$

$$N(^4S) + NO \rightarrow N_2 + O(^3P) \quad (A.5)$$

$$N(^4S) + NO_2 \rightarrow 2NO \quad (A.6)$$

$$N(^4S) + O_2 \rightarrow NO + O(^3P) \quad (A.7)$$

$$N(^4S) + O_3 \rightarrow NO + O_2 \quad (A.8)$$

$$N(^2D) + O_2 \rightarrow NO + O(^3P) \quad (A.9)$$

$$N(^2D) + NO \rightarrow N_2 + O(^3P) \quad (A.10)$$

$$O(^3P) + NO + M \rightarrow NO_2 + M \quad (A.11)$$

$$O(^3P) + NO_2 \rightarrow NO + O_2 \quad (A.12)$$

$$O(^3P) + O_2 + M \rightarrow O_3 + M \quad (A.13)$$

$$O(^3P) + NO_2 + M \rightarrow NO_3 + M \quad (A.14)$$

$$O(^3P) + NO_3 \rightarrow NO_2 + O_2 \quad (A.15)$$

$$O_3 + NO \rightarrow O_2 + NO_2 \quad (A.16)$$

$$NO + NO_3 \rightarrow 2NO_2 \quad (A.17)$$

$$2NO + O_2 \rightarrow 2NO_2 \quad (A.18)$$

$$NO_2 + O_3 \rightarrow NO_3 + O_2 \quad (A.19)$$